Article
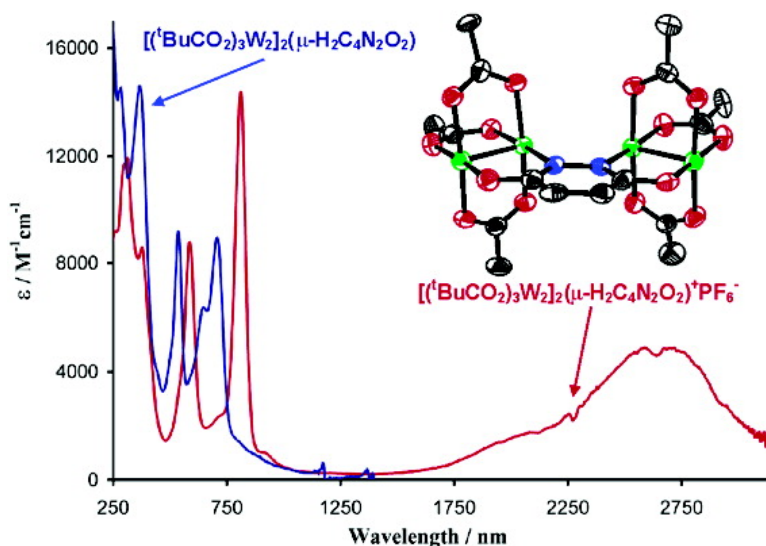
Electronically-Coupled Tungsten–Tungsten Quadruple Bonds: Comparisons of Electron Delocalization in 3,6-Dioxypyridazine and Oxalate-Bridged Compounds

Malcolm H. Chisholm, Robin J. H. Clark, Judith Gallucci, Christopher M. Hadad, and Nathan J. Patmore

More About This Article

Additional resources and features associated with this article are available within the HTML version:

- Supporting Information
- Links to the 3 articles that cite this article, as of the time of this article download
- Access to high resolution figures
- Links to articles and content related to this article
- Copyright permission to reproduce figures and/or text from this article

View the Full Text HTML

Electronically-Coupled Tungsten−Tungsten Quadruple Bonds: Comparisons of Electron Delocalization in 3,6-Dioxypyridazine and Oxalate-Bridged Compounds

Malcolm H. Chisholm,*,† Robin J. H. Clark,*,‡ Judith Gallucci,†
Christopher M. Hadad,*,† and Nathan J. Patmore†

*Contribution from the Department of Chemistry, The Ohio State University, 100 W. 18th Avenue,
Columbus, Ohio 43210-1185 and Christopher Ingold Laboratories, University College
London, 20 Gordon Street, London WC1H 0AJ, United Kingdom*

Received March 3, 2004; E-mail: Chisholm@chemistry.ohio-state.edu

Abstract: The preparation of the 3,6-dioxypyridazine-bridged tungsten complex, $[W_2(O_2C^tBu)_3]_2$-$(\mu\text{-}H_2C_4N_2O_2)$, **I**, is described, along with its single-electron oxidized cation, **I**$^+$, formed in the reaction between **I** and Ag$^+$PF$_6^-$. Compound **I** has been structurally characterized as a PPh$_3$ adduct, and **I**$^+$PF$_6^-$ as a THF solvate, by single-crystal X-ray studies. The geometric parameters of these compounds compare well with those calculated for the model compounds $[W_2(O_2CH)_3]_2(\mu\text{-}H_2C_4N_2O_2)$ and $[W_2(O_2CH)_3]_2(\mu\text{-}H_2C_4N_2O_2)^+$ by density functional theory employing the Gaussian 98 and 03 suite of programs. The calculations indicate that the two W$_2$ centers are strongly coupled by M$_2$ δ-to-bridge π-bonding, and further coupled by direct M$_2\cdots$M$_2$ bonding. Compound **I** is purple and shows an intense absorption in the visible region due to a metal-to-bridge charge transfer and, with excitation within this absorption, compound **I** exhibits pronounced resonance Raman bands associated with symmetric vibrations of the bridge and the M$_4$ unit. The cyclic voltammogram of **I** in THF, the EPR spectrum of **I**$^+$PF$_6$ in 2-MeTHF and the electronic absorption spectrum of **I**$^+$PF$_6^-$ in THF are consistent with electron delocalization over both W$_2$ units. These new data are compared with previous data for the molybdenum analogue, related oxalate-bridged compounds and closely related cyclic polyamidato-bridged Mo$_4$-containing compounds. It is proposed that, while the electronic coupling occurs principally by an electron-hopping mechanism for oxalate-bridged compounds, hole-hopping contributes significantly in the cases of the amidate bridges and that this is more important for M = Mo than for M = W. Furthermore, for Class III fully delocalized mixed-valence compounds, the magnitude of K_c, determined from electrochemical methods, is not necessarily a measure of the extent of electron delocalization.

Introduction

Interest continues in the study of mixed-valence species, particularly for compounds that may be described as "almost delocalized" at the interface of Class II and III behavior on the Robin and Day Scheme,[1] where Class III represents fully delocalized and Class II, strongly coupled. A simple measure of the relative stability of the mixed-valence state is often gleaned from electrochemical studies, following the work of Taube and Richardson.[2] Other evaluations of the degree of electronic coupling have focused on the nature of electronic near-IR transitions whose spectral shape or form in particular can be informative about the nature of the potential energy surface of mixed-valence species.[3,4] As with the now classical Creutz−Taube Ru^{II}−bridge−Ru^{III} compounds[5] and other compounds bridged by conjugated π-systems, the electronic coupling

falls off with distance as measured by electrochemistry. Recently, these types of study have been extended to dinuclear systems, wherein quadruple bonds have been linked by conjugated dicarboxylate units, the simplest of which is oxalate[6−8] and more exotic examples include tamurate and texate $[O_2C(CH=CH)_nCO_2]^{2-}$, where $n = 3$ and 4, respectively.[9,10] Recently, Cotton and co-workers extended their studies to cyclic polyamidato bridges between Mo$_2^{4+}$ centers.[11] These bridges are shown in Scheme 1 by the drawings **A**, **B**, and **C**. They noted that, while each could be viewed as corresponding stereochemically to the oxalate dianion, **D**, in terms of separation between the M$_2$ units, the electronic communication was, in all
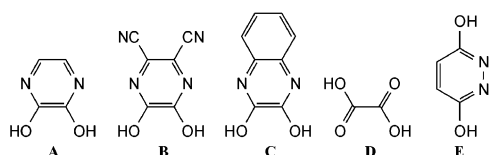
---

† Department of Chemistry, The Ohio State University.
‡ Christopher Ingold Laboratories, University College London.
(1) Robin, M. B.; Day, P. *Adv. Inorg. Radiochem.* **1967**, *10*, 247.
(2) Richardson, D. E.; Taube, H. *Inorg. Chem.* **1981**, *20*, 1278.
(3) Nelson, S. F. *Chem. Eur. J.* **2001**, *6*, 581.
(4) Brunschwig, B. S.; Creutz, C.; Sutin, N. *Chem. Soc. Rev.* **2002**, *31*, 168.
(5) Creutz, C.; Taube, H. *J. Am. Chem. Soc.* **1969**, *91*, 3988.
(6) Cayton, R. H.; Chisholm, M. H.; Huffman, J. C.; Lobkovsky, E. B. *J. Am. Chem. Soc.* **1991**, *113*, 8709.
(7) Bursten, B. E.; Chisholm, M. H.; Clark, R. J. H.; Firth, S.; Hadad, C. M.; MacIntosh, A. M.; Wilson, P. J.; Woodward, P. M.; Zaleski, J. M. *J. Am. Chem. Soc.* **2002**, *124*, 3050.
(8) Cotton, F. A.; Lin, C.; Murillo, C. A. *J. Chem. Soc., Dalton Trans.* **1998**, 3151.
(9) Cotton, F. A.; Donahue, J. P.; Murillo, C. A. *J. Am. Chem. Soc.* **2003**, *125*, 5436.
(10) Cotton, F. A.; Donahue, J. P.; Murillo, C. A.; Perez, L. M. *J. Am. Chem. Soc.* **2003**, *125*, 5486.
(11) Cotton, F. A.; Donahue, J. P.; Murillo, C. A.; Perez, L. M.; Yu, R. *J. Am. Chem. Soc.* **2003**, *125*, 8900.

Table 1. Selected Bond Lengths (Å), Angles (deg), and Torsion Angles (deg) for [(^{t}BuCO$_2$)$_3$W$_2$(PPh$_3$)]$_2$(μ-H$_2$C$_4$N$_2$O$_2$)·toluene (I) and [(^{t}BuCO$_2$)$_3$W$_2$(THF)]$_2$(μ-H$_2$C$_4$N$_2$O$_2$)(μ-THF)[pf$_6$]·THF (I$^+$PF$_6$$^-$)

I		I$^+$PF$_6$$^-$			
W1−W2	2.2028(3)	W1−W2	2.2145(2)	W5−W6	2.2162(4)
W3−W4	2.2046(3)	W3−W4	2.2183(3)	W7−W8	2.2174(4)
W2−W3	3.4333(2)	W2−W3	3.5616(2)	W6−W7	3.5588(4)
W1−P1	2.889(1)	W1−O29	2.387(6)	W5−O32	2.438(7)
W4−P2	2.856(1)	W4−O31	2.460(6)	W8−O34	2.416(6)
W1−O1	2.041(3)	W1−O1	1.997(5)	W8−O16	1.994(5)
W4−O2	2.044(3)	W4−O2	2.001(4)	W5−O15	1.997(4)
W2−N1	2.079(3)	W2−N1	2.048(5)	W7−N4	2.065(5)
W3−N2	2.074(3)	W3−N2	2.061(5)	W6−N3	2.057(5)
N1−N2	1.412(5)	N1−N2	1.434(8)	N3−N4	1.422(8)
N1−C1	1.348(6)	N1−C1	1.388(9)	N3−C35	1.374(9)
N2−C4	1.352(6)	N2−C4	1.373(5)	N4−C38	1.365(8)
O1−C1	1.322(6)	O1−C1	1.327(9)	C38−O16	1.321(8)
O2−C4	1.297(6)	O2−C4	1.350(9)	C35−O15	1.328(9)
C1−C2	1.407(7)	C1−C2	1.370(9)	C37−C38	1.371(9)
C2−C3	1.349(7)	C2−C3	1.392(9)	C36−C37	1.391(9)
C3−C4	1.404(7)	C3−C4	1.368(9)	C35−C36	1.382(9)
W2···C75	4.64(1)	O2···H36	2.618(3)	O15···H3	2.627(3)
W3···C75	4.20(1)	O11···H37	3.105(3)	O19···H2	3.155(5)
W2−W1−P1	171.27(3)	W2−W1−O29	175.2(1)	W6−W5−O32	174.8(2)
W3−W4−P2	168.17(3)	W3−W4−O31	173.1(2)	W7−W8−O34	176.1(1)
W2−N1−N2−W3	11.5(4)	W2−N1−N2−W3	0.4(6)	W7−N4−N3−W6	2.0(6)
C1−C2−C3−C4	2.7(8)	C1−C2−C3−C4	2.2(10)	C35−C36−C37−C38	0.5(10)

Scheme 1

cases, greater than that for oxalate. With the use of attendant diarylformamidinate ligands bound to the Mo$_2$ center, Cotton et al. were not able to prepare the fourth member of the cyclic amidinate series, namely a compound containing the link derived from deprotonation of 3,6-dihydroxypyridazine, **E**, in Scheme 1. We describe here our studies of W$_2$ quadruply bonded compounds containing this bridging unit which, together with earlier studies on the molybdenum analogue and oxalate compounds, provide considerable insight into the electronic coupling in these compounds. Some brief aspects of this work have been recently communicated.[12]

Results and Discussion

Synthesis. The reaction between W$_2$(O$_2$C^{t}Bu)$_4$ (2 equiv) and 3,6-dihydroxypyridazine (1 equiv) in toluene proceeds to give a fine microcrystalline powder of the compound [(^{t}BuCO$_2$)$_3$W$_2$]$_2$-(μ-H$_2$C$_4$N$_2$O$_2$), **I**. Compound **I** is air-sensitive and only sparingly soluble in hydrocarbon solvents, but appreciably soluble in donor solvents such as THF. Crystals of **I**, obtained from a THF/hexane layer, were too small for conventional laboratory single-crystal X-ray diffraction studies. In the solid state, compound **I** is most probably a coordination polymer by way of weak intermolecular W···O bonds as was seen for ditungsten oxalate and perfluoroterephthalate linked complexes.[7,13] This matter is under further investigation. However, stirring a suspension of compound **I** overnight in toluene containing a large excess of triphenylphosphine produces a clear purple solution. Layering

(12) Chisholm, M. H.; Clark, R. J. H.; Hadad, C. M.; Patmore, N. J. *Chem. Commun.* **2004**, 80.
(13) Bursten, B. E.; Chisholm, M. H.; Clark, R. J. H.; Firth, S.; Hadad, C. M.; Wilson, P. J.; Woodward, P. M.; Zaleski, J. M. *J. Am. Chem. Soc.* **2002**, *124*, 12 244.
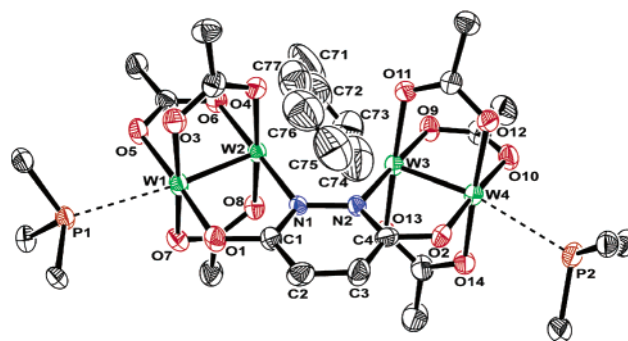
Figure 1. Crystal structure of **I**(PPh$_3$)$_2$·toluene with the anisotropic displacement parameters drawn at the 50% probability level. Only the core atoms of **I**, toluene solvate and the ipso phenyl ring carbons of PPh$_3$ are shown for clarity.

this solution with hexanes yielded single crystals of the phosphine adduct of **I**, namely [(^{t}BuCO$_2$)$_3$W$_2$(PPh$_3$)]$_2$(μ-H$_2$C$_4$N$_2$O$_2$)·toluene which were suitable for a single-crystal X-ray diffraction study.

Compound **I** reacts in THF with one equivalent of Cp$_2$Fe$^+$PF$_6$$^-$ or Ag$^+$PF$_6$$^-$ to give the oxidized cation **I$^+$** which crystallized from THF/hexane as a THF solvate [**I**(THF)$_3$]$^+$PF$_6$$^-$·THF. This compound is a blue air-sensitive material that decomposes slowly even in the solid state at room temperature (ca. 20% decomposition after 1 week as judged by UV−vis spectroscopy). It is, however, sufficiently stable to allow its characterization in solution by a variety of spectroscopic methods, and a single-crystal X-ray diffraction structure was obtained.

Solid-State and Molecular Structures. The molecular structure of **I**(PPh$_3$)$_2$·toluene is shown in Figure 1. Selected bond distances and bond angles are given in Table 1. The presence of the weak phosphine-tungsten bonds [W1−P1 = 2.889(1); W4−P2 = 2.856(1) Å] do little to perturb the electronic structure of compound **I** and are similar to those seen for W$_2$(O$_2$C^{t}Bu)$_4$(PPh$_3$)$_2$ [W−P = 2.965(3) Å].[14] The toluene

(14) Santure, D. J.; Huffman, J. C.; Sattelberger, A. P. *Inorg. Chem.* **1985**, *24*, 371.
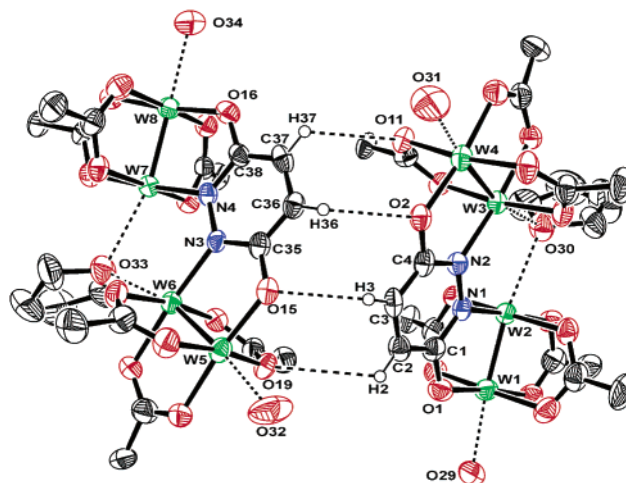
Scheme 2
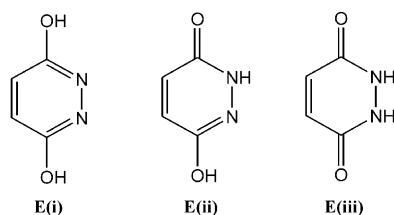
solvate is nestled in one-half of the central cavity of the molecule in close proximity to (but not significantly bonded to) the central tungsten atoms. The shortest $W-C_{(toluene)}$ bond distances are W2−C76 = 4.48(1) Å and W3−C75 = 4.20(1) Å. The other half of the cavity is occupied by a phenyl ring from a triphenylphosphine in a neighboring asymmetric unit, with the closest $W-C_{phenyl}$ contact distance of 3.947(5) Å. The $[W_2]_2$-(μ-$H_2C_4N_2O_2$) core is distorted from planarity, with a torsion angle for W2−N1−N2−W3 of 11.5(4)°. The W−W distances alternate short, long, short—corresponding to two quadruple bonds of distance 2.2028(1) and 2.2046(3) Å and a W2−W3 separation of 3.4333(2) Å. These W−W distances are shorter than that seen for $W_2(O_2C^tBu)_4(PPh_3)_2$ [2.218(1) Å],[14] although the W−O and W−N distances are as might be expected. The distances within the bridging six-membered ring are interesting. In particular, the C1−C2−C3−C4 grouping of the 3,6-dioxy-pyridazine bridging ligand shows a distinct alternation of long 1.407(7) Å, short 1.349(7) Å and long 1.404(7) Å bond distances.

There are three possible tautomers of the free ligand 3,6-dihydroxypyridazine, otherwise called maleic hydrazide, shown in Scheme 2 as **E(i)**, **E(ii)**, and **E(iii)**. Crystallographic studies have identified **E(ii)** as the only tautomer present in the solid state, having three different polymorphic forms each containing an extensive hydrogen-bonded network.[15] The alternation of long, short, long C−C distances in **I** mimics that expected for the tautomers shown in **E(i)**, **E(ii)** and **E(iii)** and seen crystallographically in polymorphs of **E(ii)**, where the average short C−C distance is 1.34 Å and the average long C−C distance is 1.43 Å. Thus, with regard to the ring π-system, the coordination to the ditungsten centers has little effect in the ground state.

The oxidized form of **I** crystallized as a THF adduct and showed disorder of the PF_6, ^tBu groups and the axially coordinated THF molecules. Despite the severe disorder in this structure there is little doubt about the connectivity of the atoms in the central W_4-containing moiety. The molecular structure of the cation in $[I(THF)_3]^+PF_6^-\cdot THF$, which contains two independent molecules that form a weakly associated dimer in the solid state by way of weak intermolecular C−H···O interactions, is shown in Figure 2. Selected bond distances are displayed alongside those of the neutral analogue in Table 1. The two axial THF molecules are weakly held as evidenced by the long W−O(THF) distances; cf., the long W−P distances in **I**, and the μ-THF ligand are reminiscent of that seen in the $(COT^1)Sc(\mu\text{-Cl})_2(\mu\text{-THF})Sc(COT^1)$ where $COT^1 = 1,4\text{-}(Me_3\text{-}Si)_2C_8H_6$.[16] The W−W distances are marginally longer (by ca. 0.014 Å) than those in **I** and the W−O and W−N distances slightly shorter. The regularity of the W−W bond lengths is consistent with a fully delocalized structure, where one electron

(15) Katrusiak, A. *Acta Crystallog. Sect. B* **2001**, *B57*, 697.
(16) Burton, N. C.; Cloke, G. N.; Hitchcock, P. B.; de Lemos, H. C.; Sameh, A. A. *Chem. Commun.* **1989**, 1462.

Figure 2. Asymmetric unit of the crystal structure of the cation $[I^+(THF)_3]_2$ with the anisotropic displacement parameters drawn at the 50% probability level. Only the core atoms of **I**$^+$ and the oxygen atoms of the axially coordinated THF molecules are shown for clarity.

has been lost in relation to **I** from the W_4 unit and not from a single W_2 core. The W−W distances thus correspond to bond orders of 3.75 for each W_2 unit. This contrasts with a recent report by Cotton et al. of valence-trapped systems involving linked Mo−Mo quadruple bonds.[17] Also of interest is the regularity of the C−C distances within the bridge. Although we do not wish to over-emphasize the importance of such a small change, we do note that it is consistent with an increase in π-donation to the tungsten atoms from the dioxypyridazine bridge. Upon oxidation, the positive charge can be delocalized onto the ligand better by the less electronegative nitrogen relative to oxygen, and there could be some π-donation from the ligand HOMO to the half-filled δ orbital of the cation **I**$^+$.

Electronic Structure and Bonding. With the intent of gaining an understanding of the electronic structure and bonding in **I** and its molybdenum analogue, we have undertaken calculations employing density functional theory with the Gaussian 98 suite of programs on the model compounds $[(HCO_2)_3M_2]_2(\mu\text{-}H_2C_4N_2O_2)$ where M = Mo or W. A vibrational frequency analysis with the optimized geometry in C_{2v} symmetry indicated that the structure was not a local minimum on the potential energy surface. Hence, the symmetry was relaxed to C_2, which was a true minimum on the potential energy surface. The fully optimized, gas-phase ground-state structure is shown in Figure 3, with the metric parameters listed in Table 2. There is close agreement between that observed experimentally for the triphenylphosphine adduct, **I**$(PPh_3)_2\cdot$toluene, and those calculated for the model compound $[(HCO_2)_3W_2]_2(\mu\text{-}H_2C_4N_2O_2)$.

Selected frontier molecular orbital plots are given in Figure 4, along with the calculated orbital energies. A more comprehensive diagram, containing all of the metal-based frontier molecular orbitals, was recently published.[12]

The frontier orbitals of the M_2 fragment for tungsten are the W−W σ, π, and δ orbitals, and these form in- and out-of-phase combinations in the W_4-containing molecules. The principal W_2−bridge−W_2 interactions arise from W_2 δ-bridge π-interactions. One W_2 δ combination is involved in back-bonding to the LUMO of the bridge π-system and this causes a splitting

(17) Cotton, F. A.; Dalal, N. S.; Liu, C. Y.; Murillo, C. A.; North, J. M.; Wang, X. *J. Am. Chem. Soc.* **2003**, *125*, 12945.
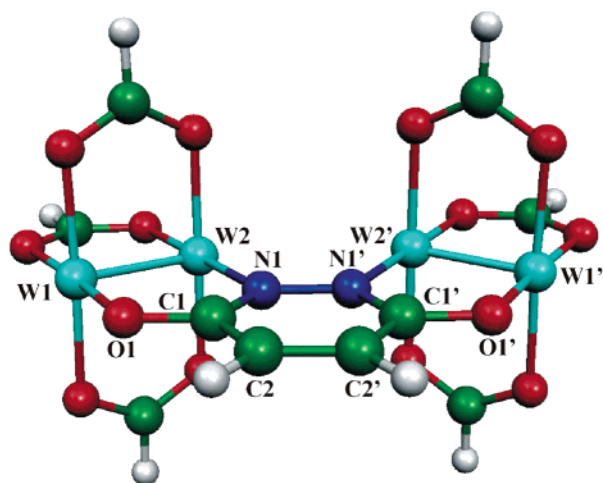
Figure 3. View of the geometry optimized structure for $[(HCO_2)_3W_2]_2$-$(\mu-N_2C_4O_2H_2)$ calculated in C_2 symmetry. Atom labels with primes are related by the C_2 axis.

Table 2. Selected Bond Lengths (Å), Angles (deg), and Torsion Angles (deg) Calculated for $[(HCO_2)_3W_2]_2(\mu-H_2C_4N_2O_2)$ (I_{calc}) and $[(HCO_2)_3W_2]_2(\mu-H_2C_4N_2O_2)^+$ (I^+_{calc})

	I_{calc}	I^+_{calc}
W1−W2	2.206	2.220
W2−W2′	3.596	3.644
W1−O1	2.050	2.024
W2−N1	2.131	2.119
O1−C1	1.305	1.309
C1−N1	1.366	1.375
N1−N1′	1.391	1.395
C1−C2	1.421	1.410
C2−C2′	1.365	1.374
W1−O1−C1	120.59	121.55
W2−N1−N1′	121.54	122.04
W2−N1−C1	119.05	118.56
O1−C1−N1	118.03	117.72
W2−N2−N2′−W2′	2.17	0.99
W1−W2−W2′−W1′	7.97	0.98
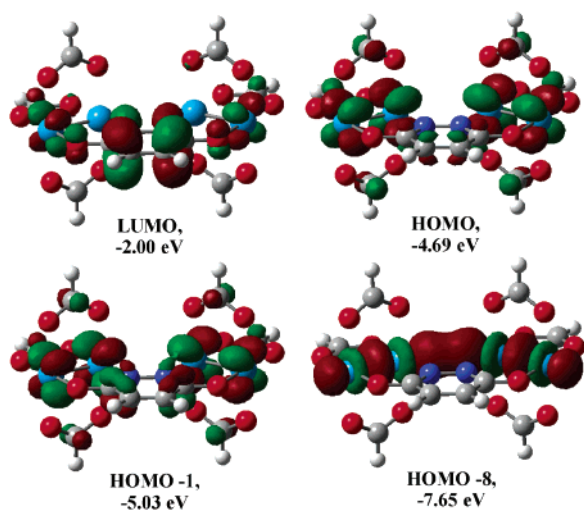
Figure 4. Selected frontier molecular orbital plots calculated for $[(HCO_2)_3W_2]_2(\mu-N_2C_4O_2H_2)$. Orbitals are drawn at an isosurface value of 0.04. The geometric orientation is the same as in Figure 3.

of the HOMO and HOMO-1 by 0.34 eV. This is a similar situation to that seen for the oxalate-bridged complex through the splitting of the δ combinations.[7] The HOMO and HOMO-1

Table 3. Calculated Frontier MO Energies for the Model Compounds $[[(HCO_2)_3M_2]_2(\mu-H_2C_4N_2O_2)$ (M = Mo, W)

frontier molecular orbital	$[(HCO_2)_3Mo_2]_2(\mu-H_2C_4N_2O_2)$		$[(HCO_2)_3W_2]_2(\mu-H_2C_4N_2O_2)$	
	MO energy/eV	assignment	MO energy/eV	assignment
HOMO-8	−7.55095	$Mo_4\ \sigma$	−7.64972	$W_4\ \sigma$
HOMO-7	−7.1572	$Mo_4\ \sigma-\pi$ hybrid	−7.07284	$W_4\ \sigma$
HOMO-6	−7.13189	$Mo_4\ \sigma-\pi$ hybrid	−6.79746	bridge π
HOMO-5	−7.0576	$Mo_4\ \pi$	−6.53976	$W_4\ \pi$
HOMO-4	−7.03012	$Mo_4\ \pi$	−6.37513	$W_4\ \pi$
HOMO-3	−6.85896	$Mo_4\ \sigma-\pi$ hybrid	−6.21295	$W_4\ \pi$
HOMO-2	−6.70548	bridge π	−6.20969	$W_4\ \pi$
HOMO-1	−5.50355	$Mo_4\ \delta$	−5.0317	$W_4\ \delta$
HOMO	−5.24694	$Mo_4\ \delta$	−4.69264	$W_4\ \delta$
LUMO	−2.23543	bridge π^*	−1.99624	bridge π^*
LUMO+1	−2.1557	$Mo_4\ \delta^*$	−1.93393	$W_4\ \sigma^*$
LUMO+2	−1.7576	$Mo_4\ \sigma^*$	−1.40575	$W_4\ \delta^*$

energy difference is smaller in the case of **I**, cf., 0.3 eV vs. 0.5 eV for the analogous oxalate-bridged compound. However, what is different is the significant splitting of the in- and out-of-phase $W_2\ \sigma$- and π-combinations. The in-phase $M_2\ \sigma$ combination at −7.65 eV (HOMO-8) is considerably lower in energy than the out-of-phase combination at −7.07 eV. As can be seen from Figure 4, this $W_4\ \sigma$-bonding orbital has considerable net $W_2\cdots W_2$ bonding. The $W_2\ \pi$-orbitals may be classified as in-plane and out-of-plane with respect to the bridge and, here again particularly for the in-plane $W_2\ \pi$-orbitals, we observe a significant energy difference between the in- and out-of-phase combinations. Specifically, compare the HOMO-5 orbital at −6.54 eV with the HOMO-2 at −6.21 eV. The HOMO-6 at −7.07 eV is a filled bridge π-MO which is principally C−N π-bonding, π_3 of the C_4N_2 six-membered ring. This orbital lies between the W−W π -and σ-combinations.

The LUMO is a bridge π-centered MO that is π_4 of the C_4N_2 ring. It is principally π-bonding between C1−C2 and C3−C4. The LUMO+1 is close in energy and can be viewed as σ_3 of the W_4 unit, being W_2 antibonding but $W_2\cdots W_2$ bonding. This is lower in energy than the $W_2\ \delta^*$- and π^*-combinations.

The bonding picture for the molybdenum analogue is qualitatively similar, and a comparison between the frontier MO energies calculated for $[(HCO_2)_3M_2]_2(\mu-H_2C_4N_2O_2)$ (M = Mo, W) is given in Figure S1 in the Supporting Information. The Mo−Mo bonding orbitals are lower in energy by ca. 0.5 eV than the corresponding W−W ones, with the result that the bridge π-bonding MO occurs below the $Mo_2\ \delta$-combinations and above the $Mo_2\ \pi$-orbitals. The HOMO and HOMO-1 are again split by interaction with the bridging π-MOs, although the splitting is smaller in the case of molybdenum than it is for tungsten (0.25 vs. 0.32 eV). The LUMO is again the bridge π^*-MO and the Mo_4-σ_3-MO, akin to that noted above for M = W, appears as the LUMO+2. In Table 3, we compare and contrast the frontier MO energies calculated for the model compounds $[(HCO_2)_3M_2]_2(\mu-H_2C_4N_2O_2)$ (M = Mo, W).

Time-dependent density functional theory calculations on the optimized geometries of these compounds were used to calculate their electronic absorption spectra. The calculations show that the lowest energy transition is the fully allowed HOMO → LUMO transition which involves metal-to-bridge charge transfer. The next electronic transition with a significant calculated oscillator strength is computed to originate primarily from a combination of the HOMO-1 to LUMO, and HOMO to LUMO+5, involving $M_4\ \delta$ to $M_4\ \pi^*$, orbital interactions.
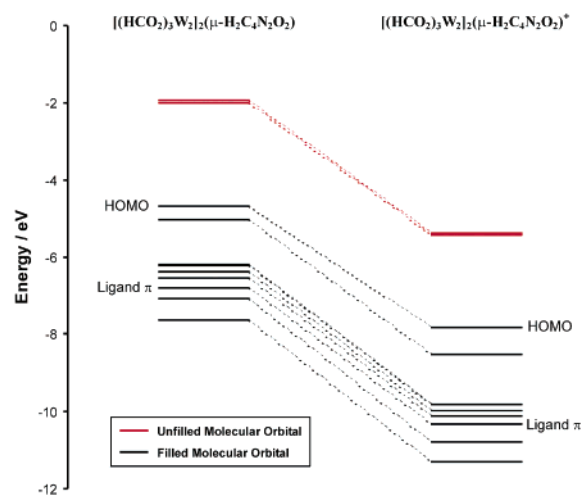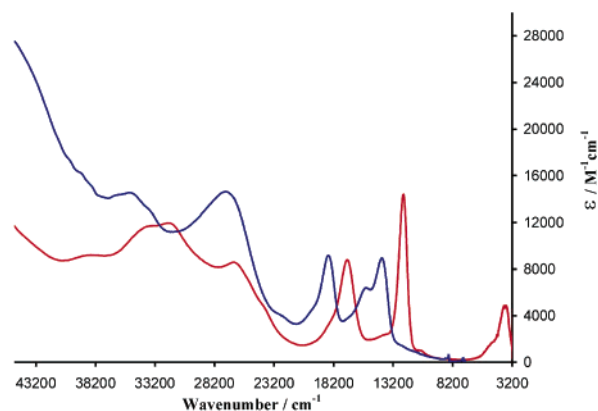
Figure 5. MO diagram comparing the relative energies of the neutral, $[(HCO_2)_3W_2]_2(\mu\text{-}H_2C_4N_2O_2)$, and oxidized, $[(HCO_2)_3W_2]_2(\mu\text{-}H_2C_4N_2O_2)^+$, species frontier molecular orbitals.

The electronic structures of the single-electron-oxidized model cations, $[(HCO_2)_3M_2]_2(\mu\text{-}H_2C_4N_2O_2)^+$ (M = Mo, W), were also calculated using unrestricted DFT calculations with the Gaussian03 suite of programs.[18] The C_2-symmetric structure for the radical cation was of ^2B symmetry and was optimized to be a minimum on the potential energy surface and verified by a vibrational frequency analysis. The metric parameters of the optimized geometries in C_2 symmetry for M = W are included alongside those of the neutral compound in Table 2, and they again show a good correlation between the theoretical, $[(HCO_2)_3W_2]_2(\mu\text{-}H_2C_4N_2O_2)^+$, and experimentally observed, $[\mathbf{I}(THF)_3]^+PF_6^-\cdot THF$, geometric results. The slight increase in the W1–W2 and W3–W4 bond lengths, in comparison to the neutral model compound, reflects the small decrease in W–W bond order from 4 to 3.75. An MO diagram comparing the calculated orbital energies of the neutral ($\mathbf{I}$) and oxidized ($\mathbf{I}^+$) model compounds is shown in Figure 5 for M = W.

Time-dependent density functional theory was used to calculate the UV–vis spectrum of the single-electron-oxidized species. The results show that the lowest energy absorbance band for $[(HCO_2)_3W_2]_2(\mu\text{-}H_2C_4N_2O_2)^+$ is the $\delta_{HOMO-1} \rightarrow \delta_{HOMO}$ transition, often termed the intervalence charge-transfer (IVCT) band, with an absorbance calculated to be in the near-IR region at 2023 nm. The next absorbance of significant intensity contains contributions from a $\delta \rightarrow \pi^*$ (MLCT) transition, as well as a $\pi \rightarrow \delta_{HOMO}$ (LMCT) transition involving the bridge.

Electronic Absorption Spectra. The electronic absorption spectrum of the purple compound $\mathbf{I}$ in THF shows a strong absorption in the visible region at 704 nm (14 205 cm^{-1}) with

(18) Frisch, M. J.; Trucks, G. W.; Schlegel, H. B.; Scuseria, G. E.; Robb, M. A.; Cheeseman, J. R.; Montgomery, J. A., Jr.; Vreven, T.; Kudin, K. N.; Burant, J. C.; Millam, J. M.; Iyengar, S. S.; Tomasi, J.; Barone, V.; Mennucci, B.; Cossi, M.; Scalmani, G.; Rega, N.; Petersson, G. A.; Nakatsuji, H.; Hada, M.; Ehara, M.; Toyota, K.; Fukuda, R.; Hasegawa, J.; Ishida, M.; Nakajima, T.; Honda, Y.; Kitao, O.; Nakai, H.; Klene, M.; Li, X.; Knox, J. E.; Hratchian, H. P.; Cross, J. B.; Adamo, C.; Jaramillo, J.; Gomperts, R.; Stratmann, R. E.; Yazyev, O.; Austin, A. J.; Cammi, R.; Pomelli, C.; Ochterski, J. W.; Ayala, P. Y.; Morokuma, K.; Voth, G. A.; Salvador, P.; Dannenberg, J. J.; Zakrzewski, V. G.; Dapprich, S.; Daniels, A. D.; Strain, M. C.; Farkas, O.; Malick, D. K.; Rabuck, A. D.; Raghavachari, K.; Foresman, J. B.; Ortiz, J. V.; Cui, Q.; Baboul, A. G.; Clifford, S.; Cioslowski, J.; Stefanov, B. B.; Liu, G.; Liashenko, A.; Piskorz, P.; Komaromi, I.; Martin, R. L.; Fox, D. J.; Keith, T.; Al-Laham, M. A.; Peng, C. Y.; Nanayakkara, A.; Challacombe, M.; Gill, P. M. W.; Johnson, B.; Chen, W.; Wong, M. W.; Gonzalez, C.; Pople, J. A. *Gaussian03*, Revision B.04 ed.; Gaussian, Inc.: Pittsburgh, PA, 2003.

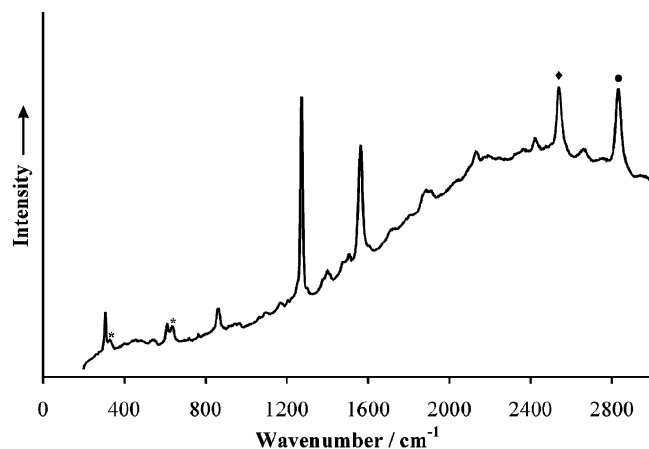**Figure 6.** UV/vis/NIR spectra of $\mathbf{I}$ (blue) and $\mathbf{I}^+PF_6^-$ (red) in THF.

evidence of a vibrational progression and an additional band centered at 535 nm (18 692 cm^{-1}). At wavelengths shorter than 300 nm, there are other intense absorptions. On the basis of the electronic structure calculations, we propose that the absorption at 704 nm arises from the HOMO-to-LUMO electronic transition which is a fully allowed metal-to-ligand (bridge) charge-transfer transition. The vibronic progression of 1360 cm^{-1} is proposed to arise from a totally symmetric ring-stretching mode which is principally $\nu(C-C)$ involving C1–C2 and C3–C4. [See Raman data presented later.] Electron transfer into the LUMO is expected to cause a significant shortening of these two C–C bonds with an attendant stretching of the other C–C (C2–C3) and C–N bonds. The higher energy absorption at 535 nm is tentatively assigned to the next transitions with significant oscillator strengths as predicted by the TDDFT calculations and is, as described earlier, a mixture of HOMO-1 to LUMO and HOMO to M_4 π^*-orbitals. The electronic absorption spectrum of $\mathbf{I}$ was also recorded in a 2-MeTHF glass at 50 K. No significant change occurred upon cooling, save that the vibrational progression seen for the absorption at 704 nm was better resolved.

The electronic spectrum of $\mathbf{I}$ is shown in Figure 6 where it is compared with that observed for the $\mathbf{I}^+$ cation in THF. The cation $\mathbf{I}^+$, which is an intense dark blue color in THF, shows bands in the visible region that are red shifted in comparison to those of the neutral compound, namely intense absorptions at 811 nm (12 330 cm^{-1}) and 585 nm (17 094 cm^{-1}). The intensity of the band at 811 nm is nearly twice that of the related transition for $\mathbf{I}$ at 704 nm and, based upon the DFT calculations, the absorption at 811 nm is now composed of both MLCT and LMCT transitions. At much lower energy, there is a broad transition centered at 2650 nm (3775 cm^{-1}) which is assigned to the IVCT transition of a fully delocalized Class III mixed-valence species. It is an a $\rightarrow$ b transition, specifically the doubly occupied HOMO-1 to singly occupied HOMO electronic transition in the radical cation.

Figure 6 clearly shows the asymmetry of the low energy transition centered at 3775 cm^{-1}, which has a width at half-height ($\Delta\tilde{\nu}_{1/2}$) of 1320 cm^{-1}. For Class II compounds, Hush theory[19] predicts that $\Delta\tilde{\nu}_{1/2} = (2310\tilde{\nu}_{max})^{1/2}$ which leads to calculated value for $\Delta\tilde{\nu}_{1/2}$ of 2950 cm^{-1} for the band at 3775 cm^{-1}. This value is much greater than the observed width, implying a Class III system.
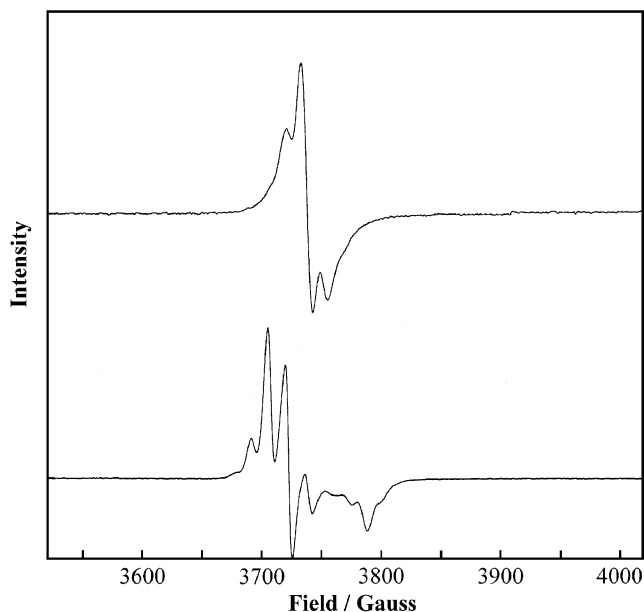
(19) Hush, N. S. *Prog. Inorg. Chem.* **1967**, *8*, 391.

Figure 7. Resonance Raman spectrum of **I** recorded with 632.8 nm excitation. Satellite peaks marked with * denote unidentified bands. Peaks marked by ♦ and ● are an overtone of the band at 1273 cm^{-1} and a combination of the 1273 and 1566 cm^{-1} bands, respectively.

Table 4. Comparison of the Observed Resonance Raman Bands of [(^{t}BuCO$_2$)$_3$W$_2$]$_2$(μ-H$_2$C$_4$N$_2$O$_2$) with Those Calculated for [(HCO$_2$)$_3$W$_2$]$_2$(μ-H$_2$C$_4$N$_2$O$_2$), and Their Assignments

experimental ν/cm^{-1}	calculated ν/cm^{-1}	assignment
308	337	W$_4$ symmetric stretch
616	633	W−O(bridge) symmetric stretch
871	882	W−W stretch and bridge "breathing"
1273	1313	symmetric bridge ring stretch
1566	1624	symmetric bridge ring stretch

Raman Spectra. With excitation at 633 nm, compound **I** shows certain resonance Raman enhanced bands and overtones as shown in Figure 7. Using 633 nm excitation, compound **I** is still absorbing photons associated with the metal-to-bridge charge transfer and it is reasonable to suppose that the resonance enhancement is associated with the vibrational modes of the bridging ligand and the M$_4$ unit. By comparison with the Raman spectrum calculated for the model compound [(HCO$_2$)$_3$W$_2$]$_2$-(μ-H$_2$C$_4$N$_2$O$_2$) in the gas phase, we propose the assignments shown in Table 4. Representations of these vibrational modes are given at http://www.chemistry.ohio-state.edu/∼chisholm/movies.html. The pronounced resonance effect seen here is good evidence for the significant structural change that occurs within the bridging ring upon photoexcitation. An examination of the nature of the LUMO predicts that the C(1)−C(2) and C(3)−C(4) distances will contract significantly on excitation thereto and the other C−C and C−N distances will respond accordingly. Excitation into the LUMO+1, which is very close in energy to the LUMO, would have a similar affect in that the W1−W2 and W3−W4 bond lengths would increase, whereas the W2··W3 distance would decrease. Hence a resonance enhancement for the band associated with the tungsten−tungsten stretch is also observed.

EPR Spectroscopy. Compound **I**$^+$PF$_6$$^-$ is paramagnetic and, according to the calculations on the model compound [(HCO$_2$)$_3$W$_2$]$_2$(μ-H$_2$C$_4$N$_2$O$_2$)$^+$, should have an unpaired electron in the M$_4$ δ combination, shown in Figure 4 as the b$_2$ HOMO orbital. The EPR spectra of the **I**$^+$ cation in 2-MeTHF at 250

Figure 8. EPR spectra of **I**$^+$PF$_6$$^-$ at 250 K (top) and as a glass at 150 K (bottom) in 2-Me-THF.

and 150 K are shown in Figure 8. At these temperatures, they represent a solution and a glass spectrum, respectively. The solution spectrum is consistent with the single electron being delocalized over four tungsten nuclei. The *g* value of 1.801 is significantly reduced from the free ion value due to spin−orbit coupling with the heavy element. Also, the existence of hyperfine coupling to ^{183}W ($I = 1/2$, 14.5% natural abundance), $A_0 = 27$ G, is indicative of the electron being in a metal-based orbital. The magnitude of the coupling is roughly half of that seen in W$_2$(O$_2$C^{t}Bu)$_4$$^+$ PF$_6$$^-$ ($A_0 = 58$ G)[20] which is consistent with the further delocalization in **I** over four tungsten nuclei, as is the relative intensity of the satellite spectrum. The satellites are not, however, well resolved. In principle, there could be two different A_0 values arising from the fact that there are two chemically different tungsten atoms. Two are bonded to oxygens and two to nitrogens of the bridging ligand, these being the outer and inner tungsten atoms of the W$_4$ chain, respectively. It is possible that this contributes to the broadness of the spectrum. Certainly the satellite spectrum is not as well resolved as that seen for the oxalate-bridged W$_4$-containing radical cation [^{t}BuCO$_2$)$_3$W$_2$]$_2$(μ-O$_2$CCO$_2$)$^+$.[21] In the frozen glass spectrum, the virtual C_{2v} symmetry of the molecular cation is revealed and a reasonable estimate of the three *g* tensors and A_0 values can be obtained ($g_x = 1.814$, $g_y = 1.808$, $g_z = 1.779$; $A_x = 28$ G, $A_y = 32$ G, $A_z = 26$ G).

Electrochemical Studies. Compound **I** in THF shows two oxidation waves, the first reversible and the second quasi reversible. The first oxidation corresponds to the formation of the cation **I**$^+$ which, as noted before, has considerable kinetic persistence. The oxidation of **I** to **I**$^+$ occurs at a lower potential ($E_{1/2}^1 = -0.91$ V) than that for the oxidation of W$_2$(O$_2$C^{t}Bu)$_4$ to W$_2$(O$_2$C^{t}Bu)$_4$$^+$ ($E_{1/2}^1 = -0.70$ V).[6] The separation between the 1st and 2nd oxidation waves is 630 mV. If this value is then used to compute a comproportionation stability constant,

(20) Chisholm, M. H.; D'Acchioli, J. S.; Pate, B. D.; Patmore, N. J., Manuscript in preparation.
(21) Chisholm, M. H.; Pate, B. D.; Wilson, P. J.; Zaleski, J. M. *Chem. Commun.* **2002**, 1084.

Table 5. Electrochemical Data and Comproportionation Constants for Selected Compounds in THF[a]

compound	$E_{1/2}^1$ (V)	$E_{1/2}^2$ (V)	$\Delta E_{1/2}$ (mV)	K_c	ref
$[(^tBuCO_2)_3Mo_2]_2(\mu\text{-}O_2C\text{-}C_6F_4\text{-}CO_2)$	+0.10		65	13	6
$[(^tBuCO_2)_3Mo_2]_2(\mu\text{-}O_2CCO_2)$	−0.03	+0.25	280	5.4×10^4	6
$[(^tBuCO_2)_3Mo_2]_2(\mu\text{-}DOP)$	−0.15	+0.28	427	1.7×10^7	22
$[(^tBuCO_2)_3W_2]_2(\mu\text{-}O_2C\text{-}C_6F_4\text{-}CO_2)$	−0.66	−0.37	285	6.6×10^4	6
$[(^tBuCO_2)_3W_2]_2(\mu\text{-}O_2CCO_2)$	−1.26	−0.54	717	1.3×10^{12}	6
$[(^tBuCO_2)_3W_2]_2(\mu\text{-}DOP)$	−0.91	−0.28	630	4.5×10^{10}	this work
$Mo_2(O_2C^tBu)_4$	−0.04				6
$W_2(O_2C^tBu)_4$	−0.70				6

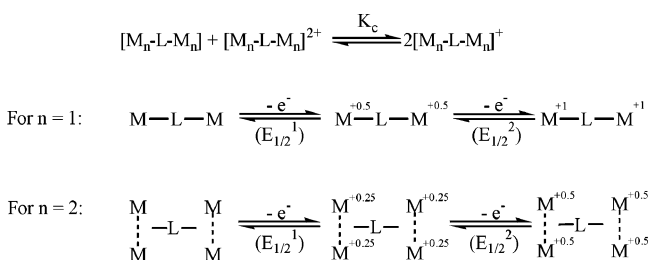[a] Oxidation potentials are referenced to the Fc$^+$/Fc couple.

K_c, for the mono cation relative to the neutral and doubly oxidized species using the Taube and Richardson equation

$$K_c = e^{\Delta E_{1/2}/25.69}$$

(where $\Delta E = 630$ mV),[2] then the mixed-valence mono cation may be classified as Class III on the Robin and Day Scheme,[1] representing a fully delocalized system with $K_c = 4.5 \times 10^{10}$. A comparison of electrochemical data is given in Table 5 for selected Mo_4 and W_4 complexes containing various bridges along with the first oxidation potentials for the parent $M_2(O_2C^t$-Bu)$_4$ complexes.

Comparisons with Oxalate-Bridged Compounds. The present work allows some significant observations to be made by comparison with the data obtained from the recent work of Cotton and earlier studies in this laboratory.[6,11,22] First, as can be gleaned from an inspection of the electrochemical data in Table 5, it is always easier to oxidize a tungsten compound relative to its molybdenum analogue and, furthermore, the magnitude of K_c always increases in going from Mo to W. Both of these effects can be traced to the energies of the $M_2 \delta$ orbitals. The higher energy of the $W_2 \delta$ orbital makes it easier to ionize and increases its orbital interactions with the LUMO of the bridge. Second, as the two M_2 centers get more strongly coupled, the 1st oxidation moves to a lower potential and K_c increases. Third, electronic coupling falls off with increasing distance between the two Mo_2 centers. This was very nicely demonstrated by Cotton et al. in the studies of $[O_2C(CH=CH)_nCO_2]^{2-}$ bridged Mo_2 quadruple bonds.[9]

The comparison with oxalate is, however, particularly pertinent in this case. The 3,6-dioxypyridazine bridge keeps the four metal atoms in one plane (or at least essentially so), and brings the metals into closer proximity. This has two noticeable effects. (1) Whereas the oxalate bridged compounds show thermochromism in 2-MeTHF solutions and glasses, the pyridazine-bridged ones do not. (2) In the oxalate-bridged complexes, the interaction between the two M_2 centers arises exclusively through the overlap of the metal δ- and the π-system of the oxalate bridge. The in-phase and out-of-phase combinations of the $M_2 \sigma$- and π-orbitals are close to being isoenergetic. In compound **I** and its Mo analogue, we see a significant interaction between the M_2 centers as a result of direct $M_2 \cdots M_2$ interactions. On the basis of this line of thought, one

(22) Cayton, R. H.; Chisholm, M. H.; Putilina, E. F.; Folting, K. *Polyhedron* **1993**, *12*, 2627.

Scheme 3

$$[M_n\text{-}L\text{-}M_n] + [M_n\text{-}L\text{-}M_n]^{2+} \overset{K_c}{\rightleftharpoons} 2[M_n\text{-}L\text{-}M_n]^+$$

For n = 1:
$$M{-}L{-}M \underset{(E_{1/2}^1)}{\overset{-\,e^-}{\rightleftharpoons}} M^{+0.5}{-}L{-}M^{+0.5} \underset{(E_{1/2}^2)}{\overset{-\,e^-}{\rightleftharpoons}} M^{+1}{-}L{-}M^{+1}$$

For n = 2:
$$\begin{matrix} M \\ | \\ M \end{matrix} {-}L{-} \begin{matrix} M \\ | \\ M \end{matrix} \underset{(E_{1/2}^1)}{\overset{-\,e^-}{\rightleftharpoons}} \begin{matrix} M^{+0.25} \\ | \\ M^{+0.25} \end{matrix} {-}L{-} \begin{matrix} M^{+0.25} \\ | \\ M^{+0.25} \end{matrix} \underset{(E_{1/2}^2)}{\overset{-\,e^-}{\rightleftharpoons}} \begin{matrix} M^{+0.5} \\ | \\ M^{+0.5} \end{matrix} {-}L{-} \begin{matrix} M^{+0.5} \\ | \\ M^{+0.5} \end{matrix}$$

would expect that the M_2 units are more strongly coupled in the 3,6-dioxypyridazine complexes than in analogous oxalate complexes. From the electrochemical data and the values of K_c for the molybdenum complexes, this appears to be true with K_c values of 10^7 vs 10^4. However, in the case of the tungsten complexes, this appears not to be true since the oxalate K_c value of $\sim 10^{12}$ is larger than that for **I**$^+$, $\sim 10^{10}$. This matter clearly warrants some further comment.

First, we may question whether it is valid to use the Taube–Richardson method to evaluate electronic coupling in mixed-valence complexes involving more than two metal centers. Consider the scenario of two clusters or nanoparticles of metal atoms connected by a ligand bridge (L) to be represented by $[M_n]{-}L{-}[M_n]$. If the bridge couples the M_n centers strongly, the removal of the first electron will be shared by $2n$ metal centers with an effective positive charge on each being $+ \frac{1}{2n}$. The second oxidation will then generate an effective positive charge of $+\frac{1}{n}$. If n is large, the difference between the $E_{1/2}$ values could obviously be very small and the computed value of K_c generated by the equation

$$K_c = e^{\Delta E_{1/2}/25.69}$$

would not be meaningful with respect to the usual assignment that $K_c > 10^6$ indicates a Class III, fully delocalized complex. In the present case, there are only four metal atoms, but the point remains that, in this type of strongly coupled system, that is delocalized or class III on the Robin and Day Scheme, the first oxidation will generate a shared positive charge with $M + 0.25$ and the second oxidation will generate $M + 0.5$, displayed diagrammatically in Scheme 3. Thus, the immediate comparison of K_c for $M_2{-}L{-}M_2$ with $M{-}L{-}M$ is not valid, and furthermore Class III behavior may be seen when K_c is considerably less than 10^6 for polynuclear systems.

The electrochemical data for oxalate and 3,6-dioxypyridazine bridge complexes still warrant an explanation as the magnitude of the $\Delta E_{1/2}$ values within pairs of related molecules are informative with regard to electron delocalization in the charged species. Cotton noted that the cyclic polyamidinate-bridged compounds of molybdenum all showed greater $\Delta E_{1/2}$ values than their oxalate counterpart, despite the fact that their Mo_2 to Mo_2 separation is essentially identical within the series.[11] For molybdenum, we also see that the 3,6-dioxypyridazine bridge yields a significantly larger K_c value, 10^7, than its oxalate counterpart 10^4. It is then worth asking why there is so little change in K_c between **I** and its molybdenum counterpart, 10^7 to 10^{10}, when for oxalate, the change is 10^4 to 10^{12}. Within each pair of compounds, solvation effects should be virtually identical as the M$-$M, $M_2 \cdots M_2$ and M$-$L bond distances are essentially the same for M = Mo and W due to the lanthanide contraction.
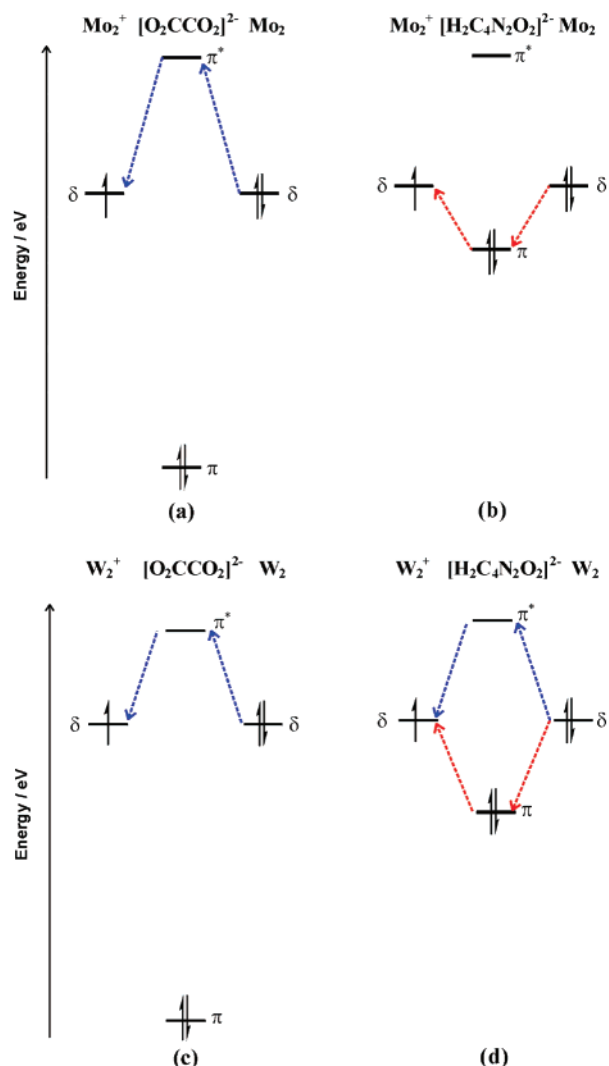
Figure 9. Qualitative Frontier MO energy level diagram depicting the relative energies of the M_2 δ (HOMO) (M = Mo, W) and the bridging ligand filled and empty π orbitals for oxalate and 3,6-dioxypyridazine, based upon calculations on the radical cation model compounds. The dotted arrow represents the energetically favored mechanism of electron delocalization via 'electron hopping' (blue) or 'hole hopping' (red).

A plausible explanation for this may lie in the mechanism of electronic communication in the two systems. For oxalate, the only significant coupling of the two M_2 centers arises through the LUMO of the oxalate dianion (Figure 9a and Figure 9c). The W_2 δ orbitals are notably closer in energy to this bridge π^* MO as evidenced by the M_4-to-bridge charge-transfer transition which occurs at 800 nm for M = W and at 460 nm for M = Mo. For the 3,6-dioxypyridazine bridge, the W_4-to-bridge CT band is at somewhat higher energy, 704 nm, and for molybdenum, around 400 nm. Thus, electron hopping might well explain why the W_4-oxalate bridged species is so strongly coupled relative to its Mo_4 counterpart but does not explain the relative difference for the 3,6-dioxypyridazine complexes. For the latter, however, the bridge π-MO of highest energy falls just below the Mo_4-δ combinations and is above the Mo_4 π's and σ's. For tungsten, this bridge π-MO is the HOMO-6, just above the W_4 σ combinations. Thus, for molybdenum, a hole-hopping mechanism should contribute significantly to the overall coupling in the radical cation (Figure 9b), whereas for tungsten, this is less important (Figure 9d). In the case of oxalate, the
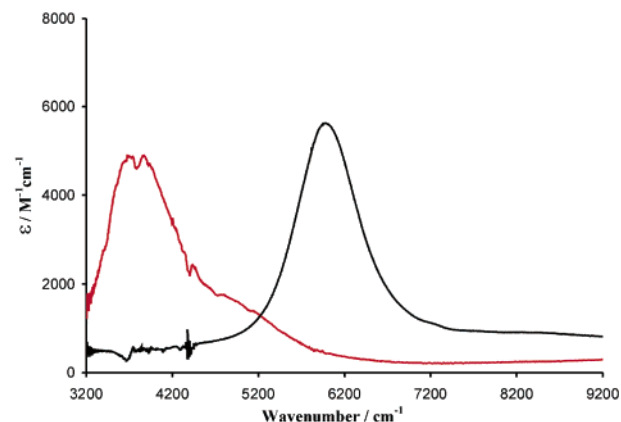
Figure 10. NIR region of the electronic absorption spectra of $\mathbf{I}^+PF_6^-$ (red) and $[(^tBuCO_2)_3W_2]_2(\mu\text{-}O_2CCO_2)^+PF_6^-$ (black).

highest energy filled π-orbital is much too low in energy to contribute significantly to a hole-hopping mechanism of electron delocalization for either molybdenum or tungsten. Schematically, this is represented in Figure 9 where the energies of the orbitals are taken from the calculation on the radical cation compounds. In reality, oxidation to the cation will stabilize the metal-based δ combinations, the HOMO and HOMO-1 relative to the bridge π-system MOs. Thus, the hole-hopping mechanism would be energetically even more favorable for molybdenum.

Another interesting comparison between the oxalate and the 3,6-dioxypyridazine-bridged complexes is that the HOMO to HOMO-1 orbital energy separation is greater for the former in the case of tungsten as a result of greater stabilization of the in-phase δ combination that interacts with the oxalate LUMO. This is seen in the calculated energies of the orbitals and in the relative energies of the IVCT bands which occur at 6000 and 3775 cm^{-1} for the oxalate and pyridazine W_4 radical cations, respectively. Much attention has been given to the nature of these low energy bands in delocalized and almost delocalized systems,[3] and it is pertinent to compare specifically these features of the 3,6-dioxypyridazine and oxalate-bridged tetra-tungsten cations, $\mathbf{I}^+$ vs $[(^tBuCO_2)_3W_2]_2(\mu\text{-}O_2CCO_2)^+$. The NIR regions of the electronic spectra of these compounds are compared in Figure 10. It is immediately apparent that these IVCT absorption bands are different both in shape and energy. The oxalate bridged cation shows a maximum intensity at the higher wavenumber, 6000 cm^{-1} vs 3775 cm^{-1}; it has a much narrower width, $\Delta\tilde{v}_{1/2} = 900$ cm^{-1} vs 1300 cm^{-1} and its shape is more Gaussian. The shape and the $\tilde{v}_{max}$ of this absorption for $\mathbf{I}^+PF_6^-$ in THF are very similar to those observed for the dimolybdenum oxalate-bridged radical cation, $[(^tBuCO_2)_3Mo_2]_2(\mu\text{-}O_2CCO_2)^+$, and for the organic tetrathiafulvalene radical cation shown in $\mathbf{F}$ below.[23]

F
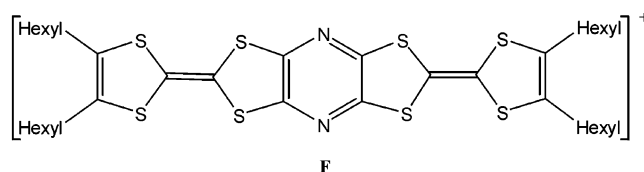
From the optical transitions, we can calculate H_{AB}, which for Class III systems is defined as $\tilde{v}_{max} = 2H$. The optical

(23) Lahlil, K.; Moradpour, A.; Bowlas, C.; Menou, F.; Cassoux, P.; Bonvoisin, J.; Launay, J.-P.; Dive, G.; Dehareng, D. *J. Am. Chem. Soc.* **1995**, *117*, 9995.

Table 6. Values of H_{AB} for Selected Class III Compounds

compound	H_{AB}/cm^{-1}	ref
[(^{t}BuCO$_2$)$_3$Mo$_2$]$_2$(μ-O$_2$CCO$_2$)$^+$PF$_6^-$	2000	21
[(^{t}BuCO$_2$)$_3$W$_2$]$_2$(μ-O$_2$CCO$_2$)$^+$PF$_6^-$	2980	21
I$^+$PF$_6^-$	1888	this work
F^a	2000	3

^{a} Originally argued to be a localized compound.[23]

parameters for **I**$^+$ and the tetratungsten oxalate radical cation are compared in Table 6 with other complexes having similar parameters. From these data, we can conclude that while both the 3,6-dioxypyridazine and oxalate bridged tetratungsten radical cations are Class III, fully delocalized, the coupling is greater for the oxalate bridge than for the pyridazine bridge, despite the difference in distance between the two dimetal units and the evidence of direct M$_2$···M$_2$ bonding in **I**$^+$PF$_6^-$.

Concluding Remarks

This work has provided the first structurally characterized examples of a bridged tungsten–tungsten quadruply bonded complex and its singly oxidized radical cation. The metric parameters indicate that, in the oxidized form, the formal charge is delocalized over all four metal centers and the W–W distances correspond to a formal bond order of 3.75. The spectroscopic data (EPR, UV/vis/NIR) and electrochemical studies support the view of Class III behavior for the radical cation. The comparison with related studies of oxalate-bridged Mo$_4$ and W$_4$ complexes is particularly illuminating, as is the comparison of electrochemical data recently reported by the Cotton group for cyclic diamidate bridges involving Mo$_4$.[11] Whereas for oxalate bridged complexes, electron delocalization occurs exclusively via an electron hopping mechanism through the bridge π*-orbitals, the introduction of the nitrogen atoms into the bridge in dihydroxypyridazine and other diamidate bridges allows for a hole hopping mechanism to contribute to delocalization. This is more facile for the molybdenum than the tungsten complexes due to the closer match in orbital energies of the M$_2$ δ and bridge π orbitals. For tungsten, electron transfer via electron hopping in the oxalate bridge is more favorable than the combined electron hopping and hole hopping transfer mechanisms that are available in the dihydroxypyridazine bridged complex. These findings should prove valuable in the selection of ligand bridges for higher order assemblies of M$_2$ units having quadruple bonds.

Experimental Section

Physical Techniques. X-band EPR spectra were recorded using a Bruker ESP300 Electron Spin Resonance spectrometer. Temperature regulation was achieved using a Bruker Variable Temperature Unit.

UV/vis/NIR spectra were recorded using a PerkinElmer Lambda 900 UV/vis/NIR spectrometer, with nitrogen purging. A 1.00 mm or 10.00 mm IR quartz cell was employed. A spectrum of the neat solvent (THF) was subtracted.

Raman spectra were recorded using a Renishaw System 1000 and its associated He/Ne laser operating at 632.8 nm using a sample of **I** packed in a capillary and sealed under an inert atmosphere.

The ^{1}H NMR spectrum of **I** was recorded on a 400 MHz Bruker DPX Avance spectrometer and referenced to residual protio signals of d$_8$-THF at δ = 3.58. Values are quoted in ppm.

The cyclic voltammogram and differential pulse voltammogram of **I** were collected at a scan rate of 100 mV s^{-1} and 5 mV s^{-1} respectively,

using a Princeton Applied Research (PAR) 173A potentiostat-galvanostat equipped with a PAR 176 current-to-voltage converter. Electrochemical measurements were performed under an inert atmosphere in a 0.5 M solution of ^{n}Bu$_4$NPF$_6$ in THF inside a single-compartment voltammetric cell equipped with a platinum working electrode, a platinum wire auxiliary electrode, and a pseudo-reference electrode consisting of a silver wire in 0.5 M ^{n}Bu$_4$NPF$_6$/THF separated from the bulk solution by a VycorTM tip. The potential values are referenced to the FeCp$_2$ / FeCp$_2^+$ couple, obtained by addition of a small amount of FeCp$_2$ to the solution.

Microanalysis was performed by Atlantic Microlab, Inc.

Synthesis. The tungsten compounds used are very air sensitive, and hence all manipulations were performed in a nitrogen-filled glovebox or by using standard Schlenk line techniques. All solvents were dried using standard procedures, and degassed prior to use. Tungsten tetrapivalate was prepared according to literature procedures.[24] Silver hexafluorophosphate and 3,6-dihydroxypyridazine were obtained from Aldrich and used without any further purification. **I**$^+$PF$_6^-$ was generated in situ for the EPR spectra by treating **I** with 0.95 equivalents of Cp$_2$Fe$^+$PF$_6^-$ in 2-Me-THF.

[(^{t}BuCO$_2$)$_3$W$_2$]$_2$(μ-H$_2$C$_4$N$_2$O$_2$) (I). A Schlenk tube was charged with 1.50 g of W$_2$(O$_2$C^{t}Bu)$_4$ (1.94 mmol) and 109 mg of 3,6-dihydroxypyridazine (0.97 mmol). Toluene (5 mL) was added and the suspension stirred for 6 days, during which time the solution turned purple. The microcrystalline product was isolated by filtration and washed with toluene (1 × 5 mL) and hexanes (2 × 5 mL) then dried in vacuo to give 835 mg (64% yield) of a purple solid. δ^1H (400 MHz, d$_8$-THF): 6.19 (2H, s), 1.34 (36H, s), 1.29 (18H, s). Microanalysis: Found, C 26.3, H 3.89, N 1.82%. Calcd. For C$_{30}$H$_{56}$N$_2$O$_{10}$W$_4$, C 26.9, H 4.21, N 2.09%.

Crystals of I(PPh$_3$)$_2$. A toluene (2 mL) solution containing a suspension of 40 mg of **I** and 200 mg of PPh$_3$ was stirred for 16 h, during which time a clear purple solution formed. This solution was layered with hexanes and placed in a freezer at −15 °C for 5 days to yield dark crystals: [(^{t}BuCO$_2$)$_3$W$_2$(PPh$_3$)]$_2$(μ-H$_2$C$_4$N$_2$O$_2$)·toluene. Attempts to isolate **I**(PPh$_3$)$_2$ in bulk from the large excess of triphenylphosphine by washing with hexanes was unsuccessful due to the high solubility of the phosphine adduct. ^{31}P NMR spectra of the mixture in d$_8$-toluene and d$_8$-THF did not show any evidence of tungsten-coordinated PPh$_3$, and the ^{1}H NMR spectrum in d$_8$-THF showed resonances at identical values to those seen for **I**.

[(^{t}BuCO$_2$)$_3$W$_2$]$_2$(μ-H$_2$C$_4$N$_2$O$_2$) $^+$PF$_6^-$ (I$^+$PF$_6^-$). A Schlenk tube was charged with 300 mg of **I** (0.22 mmol) and 57 mg of AgPF$_6$ (0.22 mmol) and THF (5 mL) added. The solution turned blue and was stirred for 1 h, then filtered through Celite. The solvent was removed in vacuo to yield 280 mg of a dark blue solid (84% yield). Crystals suitable for an X-ray diffraction study were grown by layering a sample of **I**$^+$PF$_6^-$ dissolved in THF inside a J. Young's NMR tube with hexanes. The NMR tube was placed in a freezer at −15 °C for 5 days and yielded dark crystals of [(^{t}BuCO$_2$)$_3$W$_2$(THF)]$_2$(μ-H$_2$C$_4$N$_2$O$_2$)(μ-THF)[PF$_6$]·THF.

X-ray Crystallography. The data collection crystal for **I**(PPh$_3$)$_2$·toluene was a dark brown triangular plate, while the data collection crystal for [**I**(THF)$_3$]$^+$PF$_6^-$·THF was a dark brown chunk. Examination of the diffraction pattern on a Nonius Kappa CCD diffractometer indicated a monoclinic crystal system for both crystals. All work was done at 200 K using an Oxford Cryostreams Cryostream cooler. The data collections were set up to measure a quadrant of reciprocal space with a redundancy factor of 4.1, which means that 90% of the reflections were measured at least 4.1 times. A combination of φ and ω scans with a frame width of 1.0° was used. Data integration was done with Denzo,[25] and scaling and merging of the data was done with Scalepack[25] in both instances.

(24) Santure, D. J.; Huffman, J. C.; Sattelberger, A. P. *Inorg. Chem.* **1985**, *24*.
(25) Otwinowski, Z.; Minor, W. *Methods in Enzymology, Vol 276: Macromolecular Crystallography, part A*; Carter, C. W., Jr., Sweet, R. M., Eds.; Academic Press: New York, 1997, pp 307−326.

Table 7. Crystallographic Details for **I**(PPh$_3$)$_2$·toluene and [**I**(THF)$_3$]$^+$PF$_6^-$ ·THF

	I(PPh$_3$)$_2$·toluene	[**I**(THF)$_3$]$^+$PF$_6^-$ ·THF
empirical formula	C$_{77}$H$_{94}$N$_2$O$_{14}$P$_2$W$_4$	C$_{50}$H$_{88}$F$_6$N$_2$O$_{18}$P$_1$W$_4$
formula weight	2068.88	3771.18
T (K)	200	200
wavelength (Å)	0.71073	0.71073
crystal system	monoclinic	monoclinic
space group	$P2_1$	$P2_1/c$
unit cell dimensions		
a (Å)	11.790(1)	19.915(1)
b (Å)	17.993(1)	34.809(2)
c (Å)	19.885(1)	20.334(1)
β(°)	107.295(2)	109.895(3)
V (Å^3)	4027.6(4)	13 255(1)
Z	2	8
D_{calc} (Mg m^{-3})	1.706	1.890
absorption coefficient (mm^{-1})	5.793	7.024
F(000)	2016	7288
crystal size (mm^3)	0.35 × 0.23 × 0.04	0.27 × 0.23 × 0.19
τ range for data collection (deg)	2.13−27.50	2.06−27.48
index ranges	-15 ≤ h ≤ 15, −23 ≤ k ≤ 23, −25 ≤ l ≤ 25	-25 ≤ h ≤ 25, −45 ≤ k ≤ 45, −26 ≤ l ≤ 26
reflections collected	69 012	224 111
independent reflections	18 469 [R_{int} = 0.062]	30 374 [R_{int} = 0.058]
refinement method	full-matrix least-squares on F^2	full-matrix least-squares on F^2
data/restraints/parameters	18 469/1/892	30 374/106/1312
flack parameter	0.016(5)	
goodness-of-fit on F^2	1.033	1.019
final r indices [$I > 2\sigma(I)$]	R_1 = 0.0286 wR_2 = 0.0592	R_1 = 0.0443 wR_2 = 0.1085
R indices (all data)	R_1 = 0.0355 wR_2 = 0.0614	R_1 = 0.0995 wR_2 = 0.1279
largest difference peak and hole (e/Å^3)	1.316 and −0.725	2.021 and −1.156

I(PPh$_3$)$_2$·toluene was solved by the direct methods in shelxs-97, and [**I**(THF)$_3$]$^+$PF$_6^-$·THF was solved using the Patterson method in shelxs-97.[26] Full-matrix least-squares refinements based on F^2 were performed in shelxl-97[27] in the WinGX (version 1.64.05) suite of programs.[28] All hydrogens were included in the model at calculated positions using a riding model with U(H) = 1.2 × U_{eq} (bonded carbon atom) for aromatic and methylene groups, and U(H) = 1.5 × U_{eq} (bonded carbon atom) for the methyl hydrogens.

The structure for **I**(PPh$_3$)$_2$·toluene was solved in $P2_1$, with all non-hydrogen atoms assigned anisotropic displacement parameters. The structure for [**I**(THF)$_3$]$^+$PF$_6^-$·THF was refined in $P2_1/c$. The asymmetric unit consists of two independent [**I**(THF)$_3$]$^+$PF$_6^-$·THF molecules, with the tungsten atoms related by *pseudo*-C-centering. As a result of this, the $h + k = 2n$ +1 reflections are weak. Due to disorder in the axially coordinated THF molecules and solvent THF molecules their carbon atoms were kept isotropic. In addition, several of the ^{t}Bu groups are rotationally disordered and were modeled as two isotropic sets of atoms. The fluorines on the PF$_6^-$ anions have large thermal parameters indicative of disorder, but each anion was refined in one orientation with isotropic fluorine atoms for simplicity in this large structure. Although the structure contains a large amount of disorder, involving typically disordered groups, the atoms surrounding the tungsten core are well behaved.

Experimental data relating to both structure determinations are displayed in Table 7.

Electronic Structure Calculations. Electronic structure calculations on the model compounds [(HCO$_2$)$_3$M$_2$]$_2$(μ-H$_2$C$_4$N$_2$O$_2$) (M = Mo, W) were performed using density functional theory with the aid of the Gaussian98 suite of programs.[29] The B3LYP functional[30−32] along with the 6-31G* (5d) basis set[33] were used for H, C, O, and N along with the SDD energy consistent pseudopotentials for molybdenum and tungsten.[34] Pivalate groups were substituted for formate groups in the model compounds to reduce the calculation time and allow ready comparison with previously published work.[7] Geometry optimizations were performed in C_2 symmetry as a frequency analysis on the geometry

optimization in C_{2v} symmetry showed it not to be a local minimum on the potential energy surface.

For the radical cation models, [(HCO$_2$)$_3$M$_2$]$_2$(μ-H$_2$C$_4$N$_2$O$_2$)$^+$ (M = Mo, W), spin unrestricted electronic structure calculations were performed with the aid of the Gaussian03 suite of programs[18] using the same basis sets, functionals, and pseudopotentials as outlined for the neutral analogue. Geometry optimization was performed in C_2 symmetry and verified to be a local minimum on the potential energy surface using a vibrational frequency analysis.

Orbital analyses were performed using GaussView.[35]

(26) Sheldrick, G. M. *Acta Crystallog. Sect. A* **1990**, *46*, 467.
(27) Sheldrick, G. M. "SHELXL-97," Universität Göttingen, 1997.
(28) Farrugia, L. J. *J. Appl. Crystallogr.* **1999**, *32*, 837.

(29) Frisch, M. J.; Trucks, G. W.; Schlegel, H. B.; Scuseria, G. E.; Robb, M. A.; Cheeseman, J. R.; Montgomery, J. A., Jr.; Vreven, T.; Kudin, K. N.; Burant, J. C.; Millam, J. M.; Iyengar, S. S.; Tomasi, J.; Barone, V.; Mennucci, B.; Cossi, M.; Scalmani, G.; Rega, N.; Petersson, G. A.; Nakatsuji, H.; Hada, M.; Ehara, M.; Toyota, K.; Fukuda, R.; Hasegawa, J.; Ishida, M.; Nakajima, T.; Honda, Y.; Kitao, O.; Nakai, H.; Klene, M.; Li, X.; Knox, J. E.; Hratchian, H. P.; Cross, J. B.; Adamo, C.; Jaramillo, J.; Gomperts, R.; Stratmann, R. E.; Yazyev, O.; Austin, A. J.; Cammi, R.; Pomelli, C.; Ochterski, J. W.; Ayala, P. Y.; Morokuma, K.; Voth, G. A.; Salvador, P.; Dannenberg, J. J.; Zakrzewski, V. G.; Dapprich, S.; Daniels, A. D.; Strain, M. C.; Farkas, O.; Malick, D. K.; Rabuck, A. D.; Raghavachari, K.; Foresman, J. B.; Ortiz, J. V.; Cui, Q.; Baboul, A. G.; Clifford, S.; Cioslowski, J.; Stefanov, B. B.; Liu, G.; Liashenko, A.; Piskorz, P.; Komaromi, I.; Martin, R. L.; Fox, D. J.; Keith, T.; Al-Laham, M. A.; Peng, C. Y.; Nanayakkara, A.; Challacombe, M.; Gill, P. M. W.; Johnson, B.; Chen, W.; Wong, M. W.; Gonzalez, C.; Pople, J. A. *Gaussian98*, Revision A9 ed.; Gaussian, Inc.: Pittsburgh, PA, 1998.
(30) Becke, A. D. *Phys. Rev. A* **1988**, *38*, 3098.
(31) Becke, A. D. *J. Chem. Phys.* **1993**, *98*, 5648.
(32) Lee, C.; Yang, W.; Parr, R. G. *Phys. Rev. B: Condens. Matter* **1988**, *37*, 785.
(33) Hehre, W. J.; Radom, L.; Schleyer, P. v. R.; Pople, J. A. *Ab Initio Molecular Orbital Theory*; John Wiley & Sons: New York, 1986.
(34) Andrae, D.; Haeussermann, U.; Dolg, M.; Stoll, H.; Preuss, H. *Theor. Chim. Acta* **1990**, *77*, 123.
(35) Gaussian Inc.: Pittsburgh, PA, 1998.

Supporting Information Available: CIF files for both the crystal structures reported in this paper. Comparison of the frontier MO energies for $[(HCO_2)_3Mo_2]_2(\mu\text{-}H_2C_4N_2O_2)$ and $[(HCO_2)_3W_2]_2(\mu\text{-}H_2C_4N_2O_2)$ (Figure S1). This material is available free of charge via the Internet at http://pubs.acs.org.

JA048768X